




Cite this: DOI: 10.1039/d3nr05828j

Received 16th November 2023,  
Accepted 9th January 2024

DOI: 10.1039/d3nr05828j

rsc.li/nanoscale

# Light-controlled morphological development of self-organizing bioinspired nanocomposites†

Marloes H. Bistervels,<sup>a</sup> Niels T. Hoogendoorn,<sup>a</sup> Marko Kamp,<sup>a</sup> Hinc Schoenmaker,<sup>a</sup> Albert M. Brouwer <sup>b</sup> and Willem L. Noorduin  <sup>\*,a,b</sup>

Nature's intricate biominerals inspire fundamental questions on self-organization and guide innovations towards functional materials. While advances in synthetic self-organization have enabled many levels of control, generating complex shapes remains difficult. Specifically, controlling morphologies during formation at the single micro/nanostructure level is the key challenge. Here, we steer the self-organization of barium carbonate nanocrystals and amorphous silica into complex nanocomposite morphologies by photogeneration of carbon dioxide (CO<sub>2</sub>) under ultraviolet (UV) light. Using modulations in the UV light intensity, we select the growth mode of the self-organization process inwards or outwards to form helical and coral-like morphologies respectively. The spatiotemporal control over CO<sub>2</sub> photogeneration allows formation of different morphologies on pre-assigned locations, switching between different growth modes—to form for instance a coral on top of a helix or *vice versa*, and subtle sculpting and patterning of the nanocomposites during formation. These findings advance the understanding of these versatile self-organization processes and offer new prospects for tailored designs of functional materials using photochemically driven self-organization.

## Introduction

Control over mineralization is essential for organisms to organize simple building blocks into complex morphologies with tailored functionalities.<sup>1–6</sup> For instance, biominerals comprised of calcium carbonate or calcium phosphate such as observed in mollusk shells,<sup>7</sup> skeletons,<sup>8,9</sup> and microlenses.<sup>10</sup> These biominerals can exhibit diverse morphologies that go beyond crystallographic symmetries, and are optimized in shape to fulfil specific mechanical, structural, or optical func-

tions.<sup>11</sup> Inspired by such examples, a wide range of synthetic self-organization strategies have been developed that are focused on morphological control.<sup>12–20</sup>

From this perspective, the nanocomposite morphologies that form during co-precipitation of barium carbonate (BaCO<sub>3</sub>) nanocrystals with amorphous silica (SiO<sub>2</sub>) are promising (Fig. 1).<sup>21–27</sup> This bioinspired reaction yields a wide diversity of shapes and symmetries such as vases, helices and coral-like forms that can be further sculpted and patterned by controlling the reaction conditions.<sup>28–32</sup> These morphologies show optical properties such as waveguiding and polarization.<sup>33</sup> Moreover post-process surface functionalization,<sup>34–36</sup> and ion exchange reactions have been developed towards a wide range of chemical compositions to introduce optoelectronic,<sup>37,38</sup> catalytic,<sup>39</sup> and magnetic<sup>40</sup> functionalities with preservation of the initial morphology. Control over the morphology is essential for these functionalities: *e.g.* the helical shape turns nano-

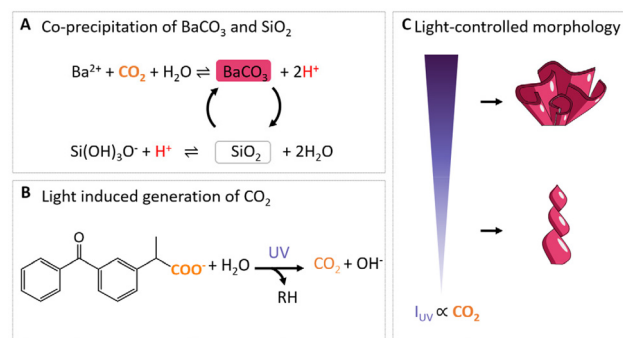


**Fig. 1** Light-controlled shaping of barium carbonate silica nanocomposites. (A) CO<sub>2</sub> induces the acid-regulated coprecipitation of BaCO<sub>3</sub> and SiO<sub>2</sub>. (B) Light-induced photodecarboxylation of ketoprofen into photoproduct RH and CO<sub>2</sub>.<sup>42</sup> (C) Hypothesis for CO<sub>2</sub> regulated morphological development in different growth modes. High *I<sub>UV</sub>* results in high CO<sub>2</sub> production such that BaCO<sub>3</sub>/SiO<sub>2</sub> composites grow outwards to the bulk solution in coral-like forms, while low values of *I<sub>UV</sub>* yield less CO<sub>2</sub> such that growth occurs inwards away from the bulk solution to form helices.

<sup>a</sup>AMOLF, Science Park 104, 1098 XG Amsterdam, The Netherlands.

E-mail: noorduin@amolf.nl

<sup>b</sup>Van 't Hoff Institute for Molecular Sciences, University of Amsterdam, Amsterdam 1090 GD, The Netherlands

† Electronic supplementary information (ESI) available. See DOI: <https://doi.org/10.1039/d3nr05828j>


composites into circular optical polarizers, while the coral-like forms offer large macroscale surfaces for maximum accessibility of the reagents and products that boosts catalytic performance.<sup>33,39,40</sup>

Recently, more refined control over the precipitation of these mineral composites was achieved by local generation of carbonate using ultraviolet (UV) light-patterns (Fig. 1B).<sup>41</sup> Specifically, photodecomposition of the organic molecule keto-profen releases carbon dioxide (CO<sub>2</sub>), which in turn can onset the coprecipitation of BaCO<sub>3</sub> and SiO<sub>2</sub>. Until now, light-induced morphological development of BaCO<sub>3</sub>/SiO<sub>2</sub> has been focused on when and where carbonate is generated. What has not been explored, is if the morphological development can be steered by how much carbonate is generated.

So far, morphological development has been controlled between two growth modes: (i) growth away from the bulk solution to form sheets, globular structures and helices, which happens at the lower pH limit (*ca.* 10.8–11.3) and increased SiO<sub>2</sub> precipitation; (ii) growth towards the bulk solution to form stems, vases and coral-like forms, which occurs at higher pH (*ca.* 11.8–12) and favors precipitation of BaCO<sub>3</sub>. Moreover, simple modulations in chemical conditions such as CO<sub>2</sub> modulations already enable further patterning and sculpting of these shapes which can be further positioned into hierarchical tectonic architectures.<sup>23</sup> The BaCO<sub>3</sub> precipitation rate is

directly determined by the concentration of CO<sub>2</sub>. Since the CO<sub>2</sub>-concentration can be controlled photochemically, this suggests that growth modes and patterns may be selected by modulating the light intensity (Fig. 1C).

Motivated by these insights we here steer the coprecipitation of BaCO<sub>3</sub>/SiO<sub>2</sub> nanocomposites by modulating the UV light intensity ( $I_{UV}$ ) to generate local CO<sub>2</sub> concentrations *via* photodecarboxylation. We demonstrate three levels of control: (1) switching between growth modes to form separate helical and coral-like structures; (2) dynamic transitioning between growth modes within a single structure; and (3) refined sculpting and patterning within one growth mode of a single structure. These results provide further insight in the role of reactions rates on morphological development of these nanocomposites, and open opportunities for tailoring self-organization towards bespoke designs of functional materials.

## Results and discussion

### Optical setup for light-controlled precipitation

Based on our previous work,<sup>41</sup> we design an optical set-up that enables UV irradiation with spatiotemporal control while simultaneously monitoring the resulting mineralization process (Fig. 2). For the UV-irradiation, we select a light emitting diode

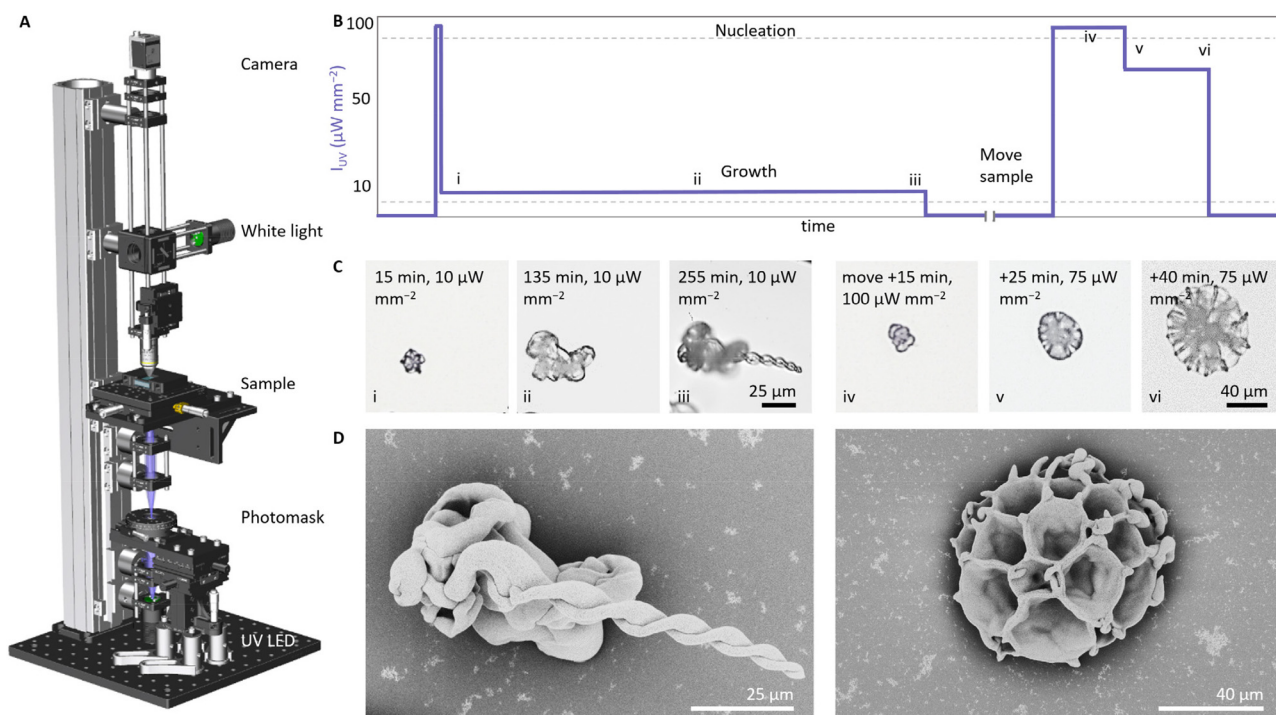


**Fig. 2** Light-controlled switching between helical and coral-like growth modes. (A) Optical setup in which UV light is focused on the reaction cell filled with the precursor solution to photochemically release CO<sub>2</sub>. Using white light, the process is monitored *in situ*. (B) Applied  $I_{UV}$  schedule to yield a helix (left), and in a different location, a coral (right): (i) nucleation is induced at high  $I_{UV}$ , (ii) growth at low  $I_{UV}$ , and (iii) stopping the precipitation by switching of  $I_{UV}$ . After moving the reaction cell to a new position, this illumination schedule is repeated: (iv) nucleation at high  $I_{UV}$  (v) growth at slightly lower  $I_{UV}$ , (v) stopping precipitation by switching off  $I_{UV}$ . The proportions of time are indicative and not to true scale. (C) Timelapse of *in situ* optical microscope images showing the growth of a helix at low  $I_{UV}$ , and growth of a coral at high  $I_{UV}$ , the indices correspond the indices in (B). (D) SEM images of the helical (left) and coral-like (right) form that are grown at low and high  $I_{UV}$  respectively.



(LED) with a wavelength of 275 nm or 365 nm, which are close to the absorption maximum of ketoprofen.<sup>42</sup> Using a photo-mask and two lenses, the UV light can be focused in a light spot with a minimum radius up to 10  $\mu\text{m}$  to irradiate a precursor solution in a reaction cell. The reaction cell—comprising two quartz plates that are separated by a Viton spacer—is positioned into a motorized and temperature-controlled sample holder. To monitor the mineralization process, an optical microscope containing a white LED, objective, and CMOS camera is positioned opposite to the UV-irradiation side.

### Light-controlled switching between growth modes

We investigate if modulations in the UV light intensity  $I_{\text{UV}}$  can determine the morphologies of the nanocomposites (Fig. 2). We fill the reaction cell with a precursor solution containing barium chloride (20 mM  $\text{BaCl}_2$ ), sodium metasilicate (9 mM  $\text{Na}_2\text{SiO}_3$ ), ketoprofen (5 mM), and dodecyl trimethylammonium bromide (50 mM DTAB, a surfactant that is added to dissolve the photoproduct of ketoprofen). Using 0.1 M HCl we lower the pH of the solution to 10.9, which in previous experiments typically resulted in the formation of helices.<sup>41</sup> Nucleation is induced by irradiating the precursor solution at high  $I_{\text{UV}}$  of  $100\ \mu\text{W}\ \text{mm}^{-2}$  for 6 seconds (UV spot has a 250  $\mu\text{m}$  radius). When the first nuclei are observed within the illuminated area, we lower  $I_{\text{UV}}$  to  $10\ \mu\text{W}\ \text{mm}^{-2}$  (255 min) to enable growth while avoiding further nucleation (Fig. 2B). As expected, we observe the formation of helical architectures, which is consistent with the typical growth in solutions of this relatively low pH (Fig. 2C and D).

We hypothesize that growth at higher  $I_{\text{UV}}$  results in a higher precipitation of  $\text{BaCO}_3$ , which in turn facilitates the formation of coral-like forms even though the low pH of the bulk solution typically favors the formation of helical shapes. To test this hypothesis, we move the sample to irradiate a new location in the reaction cell and induce new nucleation by increasing the  $I_{\text{UV}}$  to  $100\ \mu\text{W}\ \text{mm}^{-2}$  for 20 minutes. We continue growth by lowering  $I_{\text{UV}}$  to  $75\ \mu\text{W}\ \text{mm}^{-2}$  (20 min). This light intensity is 7.5 times higher than the previously used  $I_{\text{UV}}$  for growing the helical structure, but sufficiently low to avoid undesired nucleation (Fig. 2B). We observe the formation of a coral-like architecture (Fig. 2C and D). Because  $I_{\text{UV}}$  is much higher, more  $\text{CO}_2$  is generated and consequently the coral grows faster than the helix. Replicating the experiment consistently yields characteristic helical shapes for low values of  $I_{\text{UV}}$  ( $5\text{--}10\ \mu\text{W}\ \text{mm}^{-2}$ ) and coral-like shapes for high values of  $I_{\text{UV}}$  ( $50\text{--}75\ \mu\text{W}\ \text{mm}^{-2}$ ), independently of previous growth (see ESI Fig. S1 and S2†). Scanning electron microscopy (SEM) images of the corresponding morphologies confirm the development of the helical and coral-like forms. In addition, repeatedly switching between both growth modes is possible and consistently yields coral-like shapes for high  $I_{\text{UV}}$  and helices for low  $I_{\text{UV}}$  (see ESI, Fig. S2†). During this switching, we find a reduction of the nucleation rate over time, which we contribute to depletion of the precursor solution, accumulation of photoproduct, and oligomerization of silica. To compensate for this reduction in nucleation rate, we increase the photogeneration of  $\text{CO}_2$  by

increasing the  $I_{\text{UV}}$ . Hence, modulations of  $I_{\text{UV}}$  enable switching between growth modes (Fig. 2D).

### Switching growth modes within a single structure

The morphology of the growing composite is to a large extent independent of the underlying shape. This suggests that it may be possible to switch between different growth modes within a single structure by modulating  $I_{\text{UV}}$  (Fig. 3). To explore this refined control over morphological development, we prepare a precursor solution (20 mM  $\text{BaCl}_2$ , 9 mM  $\text{Na}_2\text{SiO}_3$ , 5 mM ketoprofen, 50 mM DTAB, pH 10.9). We initiate nucleation ( $100\ \mu\text{W}\ \text{mm}^{-2}$ , 18 s, 150  $\mu\text{m}$  radius) and subsequently grow a coral shape at high  $I_{\text{UV}}$  ( $75\ \mu\text{W}\ \text{mm}^{-2}$ ) (Fig. 3A). Once the coral shape is formed after 20 min (Fig. 3B, see ESI Movie 1†), we decrease  $I_{\text{UV}}$  to  $10\ \mu\text{W}\ \text{mm}^{-2}$  to reach the regime where we expect helical growth since less  $\text{CO}_2$  is generated. We continue growth in the helical growth mode for longer (*ca.* 130 min). Due to the lower concentration of  $\text{CO}_2$  most of the active growth sites on the coral shape stop growing as they become passivated with silica.<sup>43,44</sup> The parts that continue growing bend towards each other, which is characteristic for precipitation in the helical growth mode. Inspection with SEM

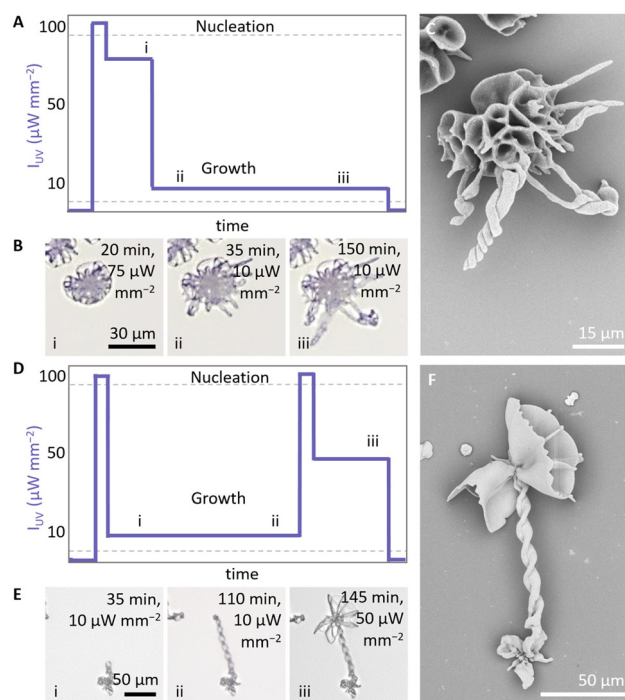


**Fig. 3** Light-controlled switching between growth modes within a single structure. (A) Indicative  $I_{\text{UV}}$  schedule for switching from (i) coral to (ii and iii) helical growth. (B) Timelapse of *in situ* optical microscope images showing the switching from a coral growth into helical forms. (C) SEM of the resulting structure. (D) Indicative  $I_{\text{UV}}$  schedule for switching from (i and ii) helical to (iii) coral growth. (E) Timelapse of *in situ* optical microscope images showing the switching from growth a helix into a coral. Indices correspond with the indices in  $I_{\text{UV}}$  schedule. (F) SEM of the resulting structure. The figures show a zoom in of the illuminated area, for a complete overview see ESI (Fig. S2– and 3†).





confirms that at the initial irradiation at high  $I_{UV}$  a coral grows, which continues in helical growth upon decreasing of  $I_{UV}$  (Fig. 3C).

To transition from helical growth to corals, we reverse the light intensity schedule (Fig. 3D). We prepare a precursor solution (20 mM  $\text{BaCl}_2$ , 11 mM  $\text{Na}_2\text{SiO}_3$ , 5 mM ketoprofen, 50 mM DTAB, pH 11.3). After nucleation at high  $I_{UV}$  ( $100 \mu\text{W mm}^{-2}$ , 25 s,  $250 \mu\text{m}$  radius), we induce helical growth at low  $I_{UV}$  ( $10 \mu\text{W mm}^{-2}$ , 110 min). Subsequently, we increase the  $\text{CO}_2$  concentration by increasing  $I_{UV}$  to  $100 \mu\text{W mm}^{-2}$  (30 s), followed by  $I_{UV}$  to  $50 \mu\text{W mm}^{-2}$  (35 min) to move into the coral growth mode. Indeed, time-lapse microscopy (Fig. 3E and ESI Movie 2†) and SEM (Fig. 3F) confirm that at low  $I_{UV}$  initially a helix forms, that subsequently transitions into a coral-like form at high  $I_{UV}$ . Modulations in  $I_{UV}$  thus enable direct switching between growth modes within a single structure.

### Light-controlled sculpting and patterning

The sensitivity of the co-precipitation process towards modulations in the  $\text{CO}_2$  concentration offers the opportunity for light-controlled shaping within a growth mode. We exemplify this capability by sculpting an architecture within the coral growth mode according to a user-defined pattern (Fig. 4). In previous research it was already shown that  $\text{CO}_2$  pulses in the bulk solution can result in sculpting and patterning.<sup>23</sup> We now investigate if local generation of  $\text{CO}_2$  still enables such control.

To demonstrate sculpting, we first induce nucleation ( $I_{UV} = 100 \mu\text{W mm}^{-2}$ , 3 s,  $250 \mu\text{m}$  radius) and growth of a coral-like structure in a precursor solution (20 mM  $\text{BaCl}_2$ , 9 mM  $\text{Na}_2\text{SiO}_3$ , 2.5 mM ketoprofen, 25 mM DTAB, pH 11.5). Once a coral form grows ( $I_{UV} = 7.5 \mu\text{W mm}^{-2}$ , 55 min), we adjust the carbonate supply by reducing  $I_{UV}$  ( $2 \mu\text{W mm}^{-2}$ , 3 min), resulting in the development of thin stems. To prevent complete passivation of growth sites by silica, we slightly increase  $I_{UV}$  ( $5 \mu\text{W mm}^{-2}$ , 45 min), and achieve a balance between carbonate supply and consumption such that stem growth is sustained. Then, we boost the local  $\text{CO}_2$  concentration and thereby trigger the splitting of the stems by applying a high intensity pulse ( $100 \mu\text{W mm}^{-2}$ , 4 s). During the splitting, the nanocrystals arrange with a wider splay, which results in an increase of the surface, as shown in Fig. 4C. Importantly, even though this high light intensity initially was also used to induce nucleation, now no new nucleation is observed as the already active growth sites deplete the local  $\text{CO}_2$  concentration. Finally, growth is continued at lower  $I_{UV}$  ( $70 \mu\text{W mm}^{-2}$ ) for 10 minutes to continue growth into vase-like forms, showing that dynamic modulations in light-intensity enable formation of complex forms.

We demonstrate patterning by forming equidistantly spaced bands on a structure. To this aim we perform short rhythmic modulations in  $I_{UV}$  using a 365 nm UV light to illuminate a small area of  $100 \mu\text{m}$  radius (Fig. 5). We prepare a precursor solution (20 mM  $\text{BaCl}_2$ , 9 mM  $\text{Na}_2\text{SiO}_3$ , 5 mM ketoprofen, 50 mM DTAB, pH 11.5). We induce nucleation using a high  $I_{UV}$  for 5 seconds ( $175 \mu\text{W mm}^{-2}$ ) and enable growth for 75 minutes at low  $I_{UV}$  ( $15 \mu\text{W mm}^{-2}$ ). To selectively enable growth on one side, we maintain the UV spot on one side of

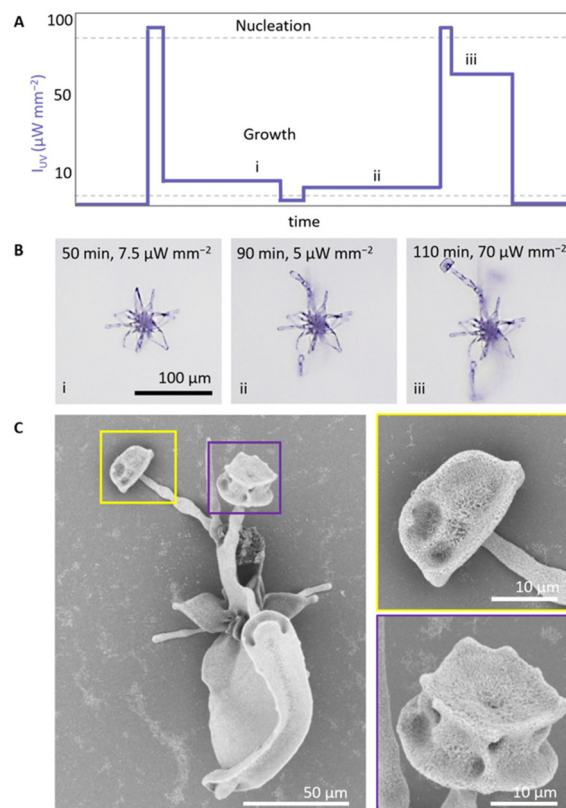


**Fig. 4** Dynamic light modulation for refined sculpting within a growth mode. (A) Indicative  $I_{UV}$  schedule. (B) Timelapse of *in situ* optical microscope images of growing architectures, showing (i) initial growth of a coral shape followed by (ii) the narrowing of the growth front to give stems at reduced  $I_{UV}$ , that subsequently (iii) open in vase-like shapes upon increasing  $I_{UV}$ , indices correspond to the indices in illumination schedule. (C) SEM images of the grown structure.

the growth front by moving the sample stage with a pace that matches the growth rate of the architecture (Fig. 5B). To form equidistantly spaced bands, we take advantage of the fact that the growth rate is approximately linear in time. To form a band, we apply a short 5 seconds pulse in  $I_{UV}$  ( $175 \mu\text{W mm}^{-2}$ ) and subsequently enable 12 minutes of growth with  $I_{UV}$  back to the original low  $I_{UV}$  ( $15 \mu\text{W mm}^{-2}$ ) before we apply another two sets of 5 seconds high  $I_{UV}$  ( $175 \mu\text{W mm}^{-2}$ ) followed by 12 minutes low  $I_{UV}$  ( $15 \mu\text{W mm}^{-2}$ ). This rhythmic light schedule of three short pulses equally paced in time results in three well-defined bands that are equally distanced in space (Fig. 5C), hence demonstrating the spatiotemporally control that can be achieved over self-organization.

### Mechanistic insights in coprecipitation reaction

Our results provide insights in the formation mechanism of  $\text{BaCO}_3/\text{SiO}_2$  nanocomposites. In well-studied configurations of  $\text{BaCO}_3/\text{SiO}_2$  coprecipitation,<sup>23,44</sup>  $\text{CO}_2$  diffuses from the air into the reaction solution. In such open systems, switching from helical to coral growth typically requires an increase of the pH from 11 to 12. Increasing the pH from 11 to 12 results in an approximate tenfold increase in  $\text{CO}_2$  that is taken up from the



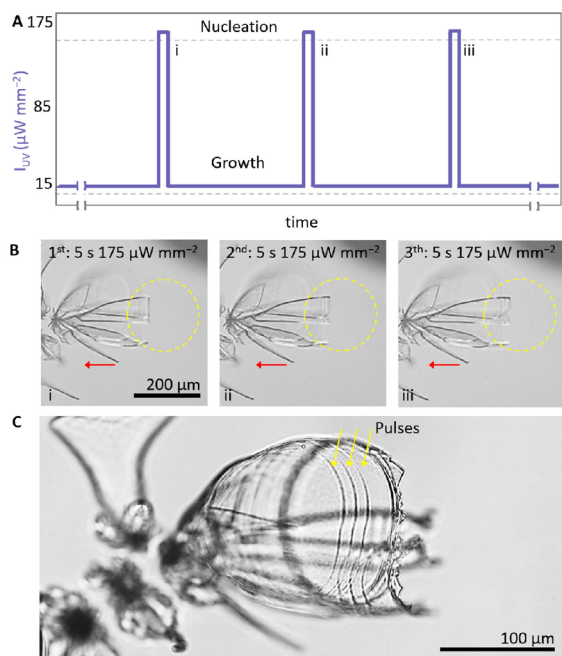


**Fig. 5** Dynamic light modulation for rhythmic patterning. (A) Selection of the indicative  $I_{UV}$  schedule, in which three short periods of 5 seconds pulses of high  $I_{UV}$  (365 nm) with 12 minutes of low  $I_{UV}$  is used to pattern a growing structure. (B) Timelapse of the growing structure after each pulse of high  $I_{UV}$ . The dashed yellow circle represents the UV spot. The red arrow indicates the direction in which the sample is moved. Indices corresponds with indices in (A). (C) Light microscope image of grown structure. The yellow arrows indicate the moments of pulses in  $I_{UV}$ .

air into the solution.<sup>45</sup> In contrast, in the closed reaction cell that we study here,  $\text{CO}_2$  is only generated photochemically in the solution. Although we are not able to determine the exact concentration of  $\text{CO}_2$  that is generated, we find that an approximate tenfold increase in  $I_{UV}$  results in switching from helices to corals. Hence both in open and closed systems an approximate tenfold increase in either  $\text{CO}_2$  uptake or  $I_{UV}$  is required to switch from helical to coral growth modes, which emphasizes the importance of the  $\text{CO}_2$  concentration in the morphological development.

The controlled local photochemical generation of  $\text{CO}_2$  also gives insights into the role of the solution pH and silica polymerization during the coprecipitation. In open systems  $\text{CO}_2$  diffusion from the air results in notable acidification of the bulk solution (typically from pH 11.8 to pH 11.5 in 2 hours). This acidification not only reduces the  $\text{CO}_2$  uptake from the air, but also induces the polymerization of silica species. The resulting silica oligomers can act as slow-diffusing species that buffer the locally acid environment around the reaction front where the co-precipitation occurs.<sup>29,30,44</sup> In the closed reaction cell,  $\text{CO}_2$  is only generated near the precipitating structures, and therefore we observe no significant change in the pH of the bulk solution. Consequently, in the closed system we need to either systematically lower the pH of the bulk (pH 10.5–10.9) or increase the silica content in the solution to access both growth modes.

These findings imply that both the silica polymerization and the  $\text{CO}_2$  concentration determine the morphological development. Overall, these findings emphasize the intricate interplay between the various components in this self-organization processes and highlight how photochemical processes can help to disentangle these processes for gaining mechanistic understanding.

## Conclusions

In this study, we show how photogeneration of  $\text{CO}_2$  can steer the morphological development of  $\text{BaCO}_3/\text{SiO}_2$  nanocomposites. With simple modulations in the light intensity, we steer the balance in the precipitation rates to switch between different growth modes, such that helical and coral-like forms can be developed in separate structures next to each other, or integrated into single structures. Moreover, we demonstrate that rational modulations in the photogeneration of  $\text{CO}_2$  enable local sculpting and patterning of structures within a single growth mode by decorating corals with thin stems that subsequently open as vases and applying rhythmic patterning. This refined level of control provides mechanistic insights and expands the possibilities for steering self-organization processes into user-defined shapes.

We foresee that these results can also impact the development of carbonate–silica nanocomposites as a platform for functional materials. Such artificial self-organization processes are still rare. However, we envisage that light-modulations can be used to steer the self-organization of components in a desired shape, after which complete chemical modification with preservation of the original morphology is possible by ion-exchange. These shape-preserving ion-exchange reactions already given access to a vast and continuously growing library of chemical compositions, which currently provide conversion routes to more than fifty different chemical compositions including perovskites, metal chalcogenides and metals.<sup>38–40,46,47,51</sup> Moreover, the catalytic, photochemical, and electronic functionalities of these bioinspired architectures have already been used, for instance as catalysts for the dry reforming of butanol at low temperatures and the Fischer-Tropsch reaction with tunable product distribution.<sup>37,38,40,46,47</sup> These results highlight the potential of combining light-controlled precipitation and conversion reactions to independently optimize shape and composition for self-organizing functional components. We also project that other self-organization processes such as Liesegang-inspired patterning or chemical gardens can be controlled using light-driven reactions.<sup>48–50</sup> As next step, integration of these self-organization and conversion principles are currently being developed.

## Experimental

### Preparation precursor solution

Typically, the precursor solution is prepared by dissolving 12.6 mg (6 mM) ketoprofen (KP) (Fluorochem) and 175.0 mg



(60 mM) DTAB (VWR) in an 8 mL aqueous solution containing 10.6 mg (11 mM) sodium metasilicate ( $\text{Na}_2\text{SiO}_3$ ) (Sigma Aldrich). Two minutes of sonication is used to enhance the dissolution of KP. In another vial, 49.5 mg barium chloride dihydrate ( $\text{BaCl}_2 \cdot 2\text{H}_2\text{O}$ ) (Sigma Aldrich) is dissolved in 2 mL degassed water (100 mM). The final precursor solution is made by adding the KP-DTAB- $\text{Na}_2\text{SiO}_3$  solution to the  $\text{BaCl}_2$  solution. The precursor solution (20 mM  $\text{BaCl}_2$ , 9 mM  $\text{Na}_2\text{SiO}_3$ , 5 mM KP, and 50 mM DTAB) is directly injected in a closed reaction cell. All solutions are kept in nitrogen during preparation to avoid any uptake of carbonate species from the air. For higher concentrations KP, a concentration ratio of 1 : 10 KP : DTAB is used to assure that both KP and the photo-product remain dissolved.

### Preparation reaction cell

The reaction cell is composed of a custom-made holder that has two quartz slides and a Viton® spacer (2–3 mm, 1.3–1.9 mL volume). The substrates are plasma cleaned for 10 minutes. Injection of the precursor solution is performed using a syringe with needle by puncturing through the Viton® spacer.

### UV-light irradiation

To induce photodecarboxylation, the sample is irradiated using UV-light irradiation of 275 nm and 365 nm and a radius of 100–250  $\mu\text{m}$ . Selection of the light intensity depends on the concentration of precursors, absorption wavelength, illumination area, and initial pH.

### UV-irradiation microscope

In the custom-built setup used for the photodecarboxylation process, we identify three main parts: the photolithography part, the sample holder stage, and the imaging part. In the irradiation part, a lens (Edmund Optics 84-337, focal length  $f = 20.0$  mm) collects the light from a 275 nm mounted LED (Thorlabs M275L4, 80 mW output power) or a 365 nm mounted LED (Thorlabs M365L3, 1290 mW output power). The UV light intensity ( $I_{\text{UV}}$  in  $\mu\text{W mm}^{-2}$ ) is determined by collecting the UV light on a handheld power meter (Thorlabs PM160T) and dividing the recorded power by the area of the sensor. Custom-made photomasks are placed after the collector lens and a light pattern is projected with the help of two UV anti-reflection coated plano-convex lenses (Thorlabs LA4148-UV,  $f = 50.0$  mm) on the sample. To control the light intensity, neutral density (ND) filters (Thorlabs NDUV-B) are used, as well as adjustments of the LED driving current. The sample holder stage consists of a custom-made temperature cell on top of a motorized translation table. The temperature is controlled by a bath and circulation thermostat (Huber CC-K6). Motion control is provided by piezo inertia actuators (Thorlabs PIAK10) that had a typical step size of 20 nm. In the imaging part, a cold white light mounted LED (Thorlabs MCWHL5) is collected by an aspheric lens (Thorlabs ACL2520U-DG6-A,  $f = 20.0$  mm). A 10 : 90 beamsplitter (Thorlabs BSN10R) directs the light through a 10×/0.30 magni-

fication objective (Nikon Plan Fluor) to the sample. The reflected images are collected with the same objective lens and transmitted through the beamsplitter. With help of a tube lens (Thorlabs AC254-200-A-ML,  $f = 200.0$  mm), images are recorded by a CMOS camera (Basler Ace acA1920-40gc).

### Post-process analysis

For post-process analysis, the cell is disassembled in degassed water by carefully separating the substrates from the spacer. The substrates are slowly pulled out of the water, while sprinkled with acetone, and subsequently dried to air. SEM imaging of the substrates is performed using a FEI Verios 460.

## Author contributions

The idea, design and concept of the research were developed by M. H. B., A. M. B. and W. L. N. The methodology was developed by M. H. B. and W. L. N. The experimental set-up was developed by M. H. B., M. K., and H. S. The experiments were performed by M. H. B. and N. T. H. The data was analyzed by M. H. B., N. T. H., and W. L. N. The project and research were managed and supervised by W. L. N. The manuscript was written and edited by M. H. B. and W. L. N.

## Conflicts of interest

The authors declare no competing interests.

## Acknowledgements

The authors thank Dr Hans Hendrikse for drawing the schematics in Fig. 1. This work is part of the Vernieuwingsimpuls Vidi research program “Shaping up materials” with project number 016.Vidi.189.083, which is partly financed by the Dutch Research Council (NWO).

## References

- 1 H. A. Lowenstam and S. Weiner, *On Biomineralization*, Oxford University Press, New York, USA, 1989.
- 2 T. Yang, H. Chen, Z. Jia, Z. Deng, L. Chen, E. M. Peterman, J. C. Weaver and L. Li, *Science*, 2022, **375**, 647–652.
- 3 A. Akiva, M. Kerschnitzki, I. Pinkas, W. Wagermaier, K. Yaniv, P. Fratzl, L. Addadi and S. Weiner, *J. Am. Chem. Soc.*, 2016, **138**, 14481–14487.
- 4 W. Huang, D. Restrepo, J. Jung, F. Y. Su, Z. Liu, R. O. Ritchie, J. McKittrick, P. Zavattieri and D. Kisailus, *Adv. Mater.*, 2019, **31**, 1–37.
- 5 P. U. P. A. Gilbert, K. D. Bergmann, N. Boekelheide, S. Tambutté, T. Mass, F. Marin, J. F. Adkins, J. Erez, B. Gilbert, V. Knutson, M. Cantine, J. O. Hernández and A. H. Knoll, *Sci. Adv.*, 2022, **8**, eabl9653.





- 6 E. Beniash, C. A. Stifler, C.-Y. Sun, G. S. Jung, Z. Qin, M. J. Buehler and P. U. P. A. Gilbert, *Nat. Commun.*, 2019, **10**, 4383.
- 7 M. Connors, T. Yang, A. Hosny, Z. Deng, F. Yazdandoost, H. Massaadi, D. Eernisse, R. Mirzaeifar, M. N. Dean, J. C. Weaver, C. Ortiz and L. Li, *Nat. Commun.*, 2019, **10**, 5413.
- 8 Y. Cui, H. Li, Y. Li and L. Mao, *Nanoscale Adv.*, 2022, **4**, 334–352.
- 9 T. Mass, A. J. Giuffre, C. Y. Sun, C. A. Stifler, M. J. Frazier, M. Neder, N. Tamura, C. V. Stan, M. A. Marcus and P. U. P. A. Gilbert, *Proc. Natl. Acad. Sci. U. S. A.*, 2017, **114**, E7670–E7678.
- 10 J. Aizenberg, A. Tkachenko, S. Weiner, L. Addadi and G. Hendler, *Nature*, 2001, **412**, 819–822.
- 11 F. C. Meldrum and H. Cölfen, *Nat. Chem.*, 2023, **15**, 1196.
- 12 M. Nakayama, S. Kajiyama, A. Kumamoto, Y. Ikuhara and T. Kato, *Nanoscale Adv.*, 2020, **2**, 2326–2332.
- 13 A. Arakaki, K. Shimizu, M. Oda, T. Sakamoto, T. Nishimura and T. Kato, *Org. Biomol. Chem.*, 2015, **13**, 974–989.
- 14 E. S. Turali-Emre, A. E. Emre, D. A. Vecchio, U. Kadiyala, J. S. VanEpps and N. A. Kotov, *Adv. Mater.*, 2023, **35**, 1–17.
- 15 U. G. K. Wegst, H. Bai, E. Saiz, A. P. Tomsia and R. O. Ritchie, *Nat. Mater.*, 2015, **14**, 23–36.
- 16 G. Isapour, B. H. Miller and M. Kolle, *Adv. Photonics Res.*, 2022, **3**, 1–7.
- 17 O. Nahi, A. N. Kulak, S. Zhang, X. He, Z. Aslam, M. A. Ilett, I. J. Ford, R. Darkins and F. C. Meldrum, *Adv. Sci.*, 2023, **10**, 1–12.
- 18 D. Nepal, S. Kang, K. M. Adstedt, K. Kanhaiya, M. R. Bockstaller, L. C. Brinson, M. J. Buehler, P. V. Coveney, K. Dayal, J. A. El-Awady, L. C. Henderson, D. L. Kaplan, S. Keten, N. A. Kotov, G. C. Schatz, S. Vignolini, F. Vollrath, Y. Wang, B. I. Yakobson, V. V. Tsukruk and H. Heinz, *Nat. Mater.*, 2023, **22**, 18–35.
- 19 M. H. Himel, B. Sikder, T. Ahmed and S. M. Choudhury, *Nanoscale Adv.*, 2022, **5**, 596–614.
- 20 Z. Xu, L. Shi, D. Hu, B. Hu, M. Yang and L. Zhu, *RSC Adv.*, 2016, **6**, 76426–76433.
- 21 J. M. García-Ruiz, E. Melero-García and S. T. Hyde, *Science*, 2009, **323**, 362–365.
- 22 M. Montalti, G. Zhang, D. Genovese, J. Morales, M. Kellermeier and J. M. García-Ruiz, *Nat. Commun.*, 2017, **8**, 1–6.
- 23 W. L. Noorduin, A. Grinthal, L. Mahadevan and J. Aizenberg, *Science*, 2013, **340**, 832–837.
- 24 C. N. Kaplan, W. L. Noorduin, L. Li, R. Sadza, L. Folkertsma, J. Aizenberg and L. Mahadevan, *Science*, 2017, **355**, 1395–1399.
- 25 M. Kellermeier, H. Cölfen and J. M. García-Ruiz, *Eur. J. Inorg. Chem.*, 2012, 5123–5144.
- 26 P. Knoll and O. Steinbock, *Isr. J. Chem.*, 2018, **58**, 682–692.
- 27 E. Nakouzi and O. Steinbock, *Sci. Adv.*, 2016, **2**, e1601144.
- 28 P. Knoll, D. S. D'Silva, D. I. Adeoye, M. G. Roper and O. Steinbock, *ChemSystemsChem*, 2021, **3**, e2000061.
- 29 T. Terada, S. Yamabi and H. Imai, *J. Cryst. Growth*, 2003, **253**, 435–444.
- 30 E. Bittarello and D. Aquilano, *Eur. J. Mineral.*, 2007, **19**, 345–351.
- 31 J. Opel, M. Kellermeier, A. Sickinger, J. Morales, H. Cölfen and J. M. García-Ruiz, *Minerals*, 2018, **8**, 1–12.
- 32 M. Kellermeier, F. Glaab, A. M. Carnerup, M. Drechsler, B. Gossler, S. T. Hyde and W. Kunz, *J. Cryst. Growth*, 2009, **311**, 2530–2541.
- 33 L. Helmbrecht, M. Tan, R. Röhrich, M. H. Bistervels, B. O. Kessels, A. F. Koenderink, B. Kahr and W. L. Noorduin, *Adv. Funct. Mater.*, 2020, **30**, 1–5.
- 34 J. Opel, J. Brunner, R. Zimmermanns, T. Steegmans, E. Sturm, M. Kellermeier, H. Cölfen and J. M. García-Ruiz, *Adv. Funct. Mater.*, 2019, **29**, 1–7.
- 35 J. Opel, F. P. Wimmer, M. Kellermeier and H. Cölfen, *Nanoscale Horiz.*, 2016, **1**, 144–149.
- 36 J. Opel, L. C. Rosenbaum, J. Brunner, A. Staiger, R. Zimmermanns, M. Kellermeier, T. Gaich, H. Cölfen and J. M. García-Ruiz, *J. Mater. Chem. B*, 2020, **8**, 4831–4835.
- 37 B. C. Batista and O. Steinbock, *Chem. Commun.*, 2022, **58**, 12736–12739.
- 38 T. Holtus, L. Helmbrecht, H. C. Hendrikse, I. Baglai, S. Meuret, G. W. P. Adhyaksa, E. C. Garnett and W. L. Noorduin, *Nat. Chem.*, 2018, **10**, 740–745.
- 39 H. C. Hendrikse, A. Aguirre, A. Van Der Weijden, A. S. Meeussen, F. Neira D'Angelo and W. L. Noorduin, *Cryst. Growth Des.*, 2021, **21**, 4299–4304.
- 40 H. C. Hendrikse, A. van der Weijden, M. Ronda-Lloret, T. Yang, R. Bliem, N. R. Shiju and M. van Hecke, *Adv. Mater.*, 2020, **32**, 2003999.
- 41 M. H. Bistervels, M. Kamp, H. Schoenmaker, A. M. Brouwer and W. L. Noorduin, *Adv. Mater.*, 2022, **34**, 2107843.
- 42 G. Cosa, L. J. Martínez and J. C. Scaiano, *Phys. Chem. Chem. Phys.*, 1999, **1**, 3533–3537.
- 43 J. Opel, M. Hecht, K. Rurack, J. Eiblmeier, W. Kunz, H. Cölfen and M. Kellermeier, *Nanoscale*, 2015, **7**, 17434–17440.
- 44 M. Kellermeier, E. Melero-García, F. Glaab, J. Eiblmeier, L. Kienle, R. Rachel, W. Kunz and J. M. García-Ruiz, *Chem. – Eur. J.*, 2012, **18**, 2272–2282.
- 45 W. J. Cai, Y. Y. Xu, R. A. Feely, R. Wanninkhof, B. Jönsson, S. R. Alin, L. Barbero, J. N. Cross, K. Azetsu-Scott, A. J. Fassbender, B. R. Carter, L. Q. Jiang, P. Pepin, B. Chen, N. Hussain, J. J. Reimer, L. Xue, J. E. Salisbury, J. M. Hernández-Ayón, C. Langdon, Q. Li, A. J. Sutton, C. T. A. Chen and D. K. Gledhill, *Nat. Commun.*, 2020, **11**, 1–13.
- 46 H. C. Hendrikse, S. Hémon-Charles, L. Helmbrecht, E. P. Van Dam, E. C. Garnett and W. L. Noorduin, *Cryst. Growth Des.*, 2021, **21**, 4500–4505.
- 47 Q. Wang and O. Steinbock, *Phys. Chem. Chem. Phys.*, 2022, **24**, 14538–14544.
- 48 B. C. Batista, A. Z. Morris and O. Steinbock, *Proc. Natl. Acad. Sci. U. S. A.*, 2023, **120**, e2305172120.



- 49 C. T. van Campenhout, H. Schoenmaker, M. van Hecke and W. L. Noorduin, *Adv. Mater.*, 2023, **2305191**, 1–8.
- 50 L. M. Barge, S. S. S. Cardoso, J. H. E. Cartwright, G. J. T. Cooper, L. Cronin, A. De Wit, I. J. Doloboff, B. Escribano, R. E. Goldstein, F. Haudin, D. E. H. Jones, A. L. Mackay, J. Maselko, J. J. Pagano, J. Pantaleone, M. J. Russell, C. I. Sainz-Díaz, O. Steinbock, D. A. Stone, Y. Tanimoto and N. L. Thomas, *Chem. Rev.*, 2015, **115**, 8652–8703.
- 51 van der Weijden, Contraction and Expansion of Nanocomposites during Ion Exchange Reactions, *Cryst. Growth Des.*, 2022, **22**, 2289–2293, DOI: [10.1021/acs.cgd.1c01364](https://doi.org/10.1021/acs.cgd.1c01364).

